A NUMERICAL DESIGN STUDY FOR ACTIVE FLOW CONTROL ON INLETS OF UHBR ENGINE NACELLES

S. Hayböck*, H. Abdellah*, C. Breitsamter*

* Technical University of Munich, Chair of Aerodynamics and Fluid Mechanics, Boltzmannstr. 15, 85748 Garching, Germany

Abstract

Innovative nacelle designs and disruptive technologies are required to minimize drag and weight penalties of high bypass ratio turbofan engines. Active flow control can improve flow quality at the aerodynamic interface plane while significantly reducing structural weight and drag through more aggressive, i.e., shorter inlet geometries. In this work, the design of an active flow control system on a future wind tunnel model is numerically investigated. Unsteady Reynolds-Averaged Navier-Stokes simulations are conducted at an angle of attack of $\alpha = 29°$ and a free-stream Mach number of $Ma_\infty = 0.15$. In this initial design phase, blowing is performed steadily with constant mass flow. Possible interactions between the fan and the inlet flow are neglected. Thus, the nacelle is modeled as a generic flow-through nacelle. A sensitivity analysis evaluates the effects of predefined design parameters of the system on inlet performance, starting from a baseline configuration of the active flow control system. Stepwise optimization of parameters significantly improves inlet-specific flow homogeneity coefficients DC_{60} and SC_{60} by up to 26.3% and 18.2%, respectively. Further, a flow field analysis reveals that, given a proper choice of parameters, counter-rotating pairs of vortices form downstream of the blowing ports, improving inlet performance considerably.

Keywords

active flow control; short intake; nacelle aerodynamics

NOMENCLATURE

Symbols

α	angle of attack	deg
α_{jet}	pitch angle	deg
β_{jet}	skew angle	deg
η_σ	pressure recovery coefficient	-
κ	curvature	1/m
θ	circumferential angle	deg
c	chord length	m
C_D	drag coefficient	-
C_L	lift coefficient	-
c_p	pressure coefficient	-
d	diameter	m
DC_{60}	distortion coefficient	-
l	length	m
Ma	Mach number	-
p	static pressure	Pa
p_t	total pressure	Pa
q	dynamic pressure	Pa
r	radius	m
SC_{60}	swirl coefficient	-
U	velocity magnitude	m/s
u, v, w	velocity components	m/s
u_c	circumferential velocity	m/s

Subscripts

60	in a sector of 60°
∞	freestream/ambient conditions
bl	baseline
fan	fan-face
hl	highlight
int	inlet
nac	nacelle
opt	optimized
th	throat

Acronyms

AFC	active flow control
AIP	aerodynamic interface plane
CVP	counter-rotating vortex pair
RANS	Reynolds-Averaged Navier-Stokes
UHBR	ultra-high bypass ratio

1. INTRODUCTION

Today's environmental challenges demand a climate-friendly future for aviation. Turbofan engines are moving towards higher bypass ratios and larger fan diameters to increase propulsive efficiency. Large bypass ratios and fan diameters of modern, fuel-efficient turbofan engines result in higher weight and drag due to a bigger nacelle surface and longer inlet sections. As early as 1990, Zimbrick and Colehour [1] discussed the need for shorter than conventional inlets to counteract drag and weight penalties of ultra-high bypass ratio (UHBR) engine nacelles. In a numerical parameter study, Peters et al. [2] found a 16% reduction in nacelle drag for a short-inlet design with an inlet length over fan diameter ratio of L/D = 0.25 compared to the standard configuration with L/D = 0.5. Aerodynamic limitations for short inlets are the interaction of the fan rotor with over-speed regions at the inlet lip and reduced flow straightening. These mechanisms can cause increased flow distortion and reduced fan efficiency relative to conventional inlets. Freeman and Rowe [3] experimentally investigated inlet engine interactions of a large turbofan engine. They found that inlet separation and non-uniform pressure distribution raise the fan's operating line, and eventually, the fan could experience rotating stall. Lee et al. [4] performed unsteady full annulus simulations under crosswind to analyze aerodynamic instabilities on a modern low-speed fan rig. Inlet separation and a significant loss in stall margin were observed for sufficiently high levels of crosswind. In addition, fan stability was found to be less sensitive to inlet distortions at higher rotational speeds due to flow acceleration upstream of the fan face.

Active flow control (AFC) can prevent stall and engine surge at off-design conditions by ensuring inflow quality measures specified by engine manufacturers. The term "active flow control" suggests introducing additional energy into the flow through an actuator system and offers advantages over passive systems [5]. Active control can be deactivated when not needed and adjusted to changing flight conditions. Local air injection at the inlet lip can help to energize and stabilize the boundary layer, increasing the aerodynamic load capacity of engine inlets far beyond current levels. Especially in climb and crosswind conditions, preventing boundary layer separation can increase pressure recovery and reduce distortion values at the aerodynamic interface plane (AIP).

The following quantities are used to evaluate the quality of the inlet flow in this parameter study. The pressure recovery coefficient η_σ describes the inlet efficiency [6].

$$\eta_\sigma = \frac{p_{t,AIP} - p_\infty}{q_\infty} \tag{1}$$

It is defined as the ratio of the average total pressure at the AIP $p_{t,AIP}$ minus the ambient pressure p_∞ divided by the dynamic pressure of the undisturbed flow $q_\infty = 1/2 \rho U_\infty^2$. The distortion coefficient DC_{60} is commonly used to evaluate the total pressure distortion at the AIP.

$$DC_{60} = \frac{p_{t,AIP} - p_{t,min,60}}{q_{AIP}} \tag{2}$$

It gives the difference between the average total pressure at the AIP $p_{t,AIP}$ and the minimum average total pressure $p_{t,min,60}$ in a segment of $60°$ at the AIP divided by the average dynamic pressure at the AIP q_{AIP}. A secondary effect of flow separation is often a high angular swirl. Guo and Seddon [6] proposed a swirl coefficient SC_{60}.

$$SC_{60} = \frac{u_{c,max,60}}{u_{AIP}} \tag{3}$$

It is the quotient of the maximum average circumferential velocity $u_{c,max,60}$ in a segment of 60° and the average velocity in x-direction at the AIP u_{AIP}.

AFC has already proven to be effective on inlet flows in the past. For example, Gorton et al. [7] successfully applied AFC in wind tunnel tests on an S-duct inlet of a blended-wing-body concept aircraft, reducing inlet distortions from a DC_{60} value of 0.29 to 0.046. Delot et al. [8] experimentally tested continuous and pulsed blowing on a high offset intake diffuser and showed up to 50% improvement in DC_{60} level. The spatial orientation of the jets, the actuator frequency, and the jet velocity are crucial for the system's overall effectiveness. In a study by Garnier [9], a spectral analysis was carried out on continuous and pulsed supersonic jets in a curved S-duct inlet. Continuous blowing was found to be a more effective operation state for reattaching the separated flow. According to the author, using the natural frequencies of the uncontrolled, separated flow as actuator frequencies is not recommended. Nambiar and Pachidis [10] did a numerical study on lip blowing on a NASA Common Research Model type engine nacelle at medium to high angles of attack. Continuous circumferential slots in different shapes were located just after the inlet throat, extending 45° from the nacelle's symmetry plane at the bottom inlet section on both sides. Blowing was performed perpendicular to the inlet surface and at an angle of 45°. Wider slots providing a higher mass flow rate and inclined slots were generally found to be more effective than thinner slots blowing perpendicularly. Here, a comprehensive parameter study is conducted on a similar engine inlet, analyzing the effect of circular jets in various orientations and arrangements.

The paper is structured as follows. Section 2 describes the design of the generic flow-through nacelle, including the chosen parameterization approach for the nacelle and its blowing ports. The numerical setup is discussed in section 3, where attention is also given to the validation measures taken. Section 4 provides findings of the sensitivity analysis of AFC design parameters and the results of the subsequent optimization steps. Further, Section 4 gives information on prevailing flow phenomena through analysis of the flowfield. Section 5 summarizes the results and gives an outlook on possible future work.

2. MODEL DESIGN

2.1. Nacelle Geometry

A custom parameterization tool was developed for the design of the inlet and outer hull of the nacelle, which is based on the Hybrid intuitive Class Shape Transformation (HiCST) from Christie et al. [11]. Kulfan and Bussoletti [12] pioneered this method by mathematically representing the shapes of aircraft components. Instead of using a large number of coordinates, a simple class function of the form $C(x/c) = \sqrt{x/c}\cdot(1-x/c)$ represents the rough geometry, and a shape function defines arbitrary 2D and 3D geometries. To fully describe the smooth profile curve of a dimensionless, axisymmetric nacelle geometry, 14 characteristic parameters are needed. The fan radius r_{fan} is an extra, dimensionally dependent parameter that determines the spatial extension of the nacelle. Table 1 lists all dimensionless parameters, along with their formula definitions, descriptions, and chosen values. The parameterization tool uses characteristic quantities of an engine nacelle, illustrated in Fig. 1. These parameters closely represent the shape of nacelles on short-inlet turbofan engines. The L/D ratio of the inlet is 0.34, which is significantly lower than typical L/D ratios of current long-range aircraft engines. The diffuser angle downstream of the throat is slightly larger than in current inlet designs. As a result, the bottom lip section experiences premature inlet flow separation at lower angles of attack, especially relevant to study the effects of AFC on flow separation. A spline with four support points defines the inner section between the fan face and the trailing edge of the profile.

Two criteria were considered when determining the size of the nacelle. The largest possible model size is advantageous for future wind tunnel tests to address sufficiently large Reynolds numbers and provide sufficient installation space for instrumentation inside the model. The maximum size of the model is limited by the blockage of the measurement section in the wind tunnel, which can be assessed by the ratio of the highlight area $A_{hl} = r_{hl}^2\pi$ and the cross-section area of the wind tunnel A_{WT}. Blockage A_{hl}/A_{WT} should be kept below 7%. Thus, the fan radius is set to $r_{fan} = 0.285$ m for the numerical design study, resulting in a blockage of 6.5%. Hence, the radius at the highlight r_{hl} measures 0.3 m, and the chord length of the nacelle $c = l_{nac}$ is 0.81 m.

Param.	Formula	Description	Value
AR_{nac}	l_{nac}/r_{hl}	nacelle aspect ratio	2.7
$f_{r,max}$	r_{max}/r_{hl}	maximum radius	1.175
f_{max}	l_{max}/l_{nac}	location max. radius	0.3
β_{te}	–	boattail angle	11°
f_{nose}	r_{nose}/r_{hl}	nose radius cowling	0.04
f_{te}	r_{te}/r_{hl}	trailing edge radius	0.95
$f_{r,fan}$	r_{fan}/r_{hl}	fan radius	0.95
f_{il}	$r_{il}\cdot b/a^2$	initial lip radius	0.4
L/D	l_{int}/d_{fan}	length diameter ratio	0.34
$f_{\kappa,th}$	$\kappa_{th}\cdot r_{hl}$	curvature at throat	5
γ_{fan}	–	wall angle at fan	-3°
$f_{\kappa,fan}$	$\kappa_{fan}\cdot r_{hl}$	curvature at fan	-1
AR	b/a	inlet aspect ratio	2
CR	$(r_{hl}/r_{th})^2$	inlet contraction ratio	1.2

TAB 1. List of characteristic parameters used to generate the generic axisymmetric nacelle geometry.

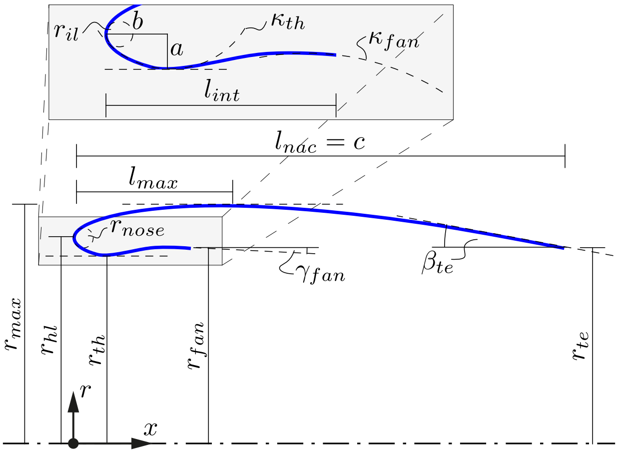

FIG 1. Display of the characteristic quantities used in the parameterization tool. The zoom window at the top gives a detailed view of the inlet section.

2.2. Flow Control Characteristics

For this design study, the AFC system can be characterized by nine parameters. The shape of the blowing ports is set to circular. Figure 2 illustrates a possible layout of the flow control system with several parameters inserted. The parameter N_{jet} determines the number of blowing ports in the half-model configuration. The two angles, θ_1 and θ_2, define the distribution of the blowing ports in circumferential direction, the former describing the angular spacing between two pairs of ports and the latter the angular spacing within a pair. The location of the blowing ports in the x-direction is specified by the parameter x_{jet}/l_{int}. The

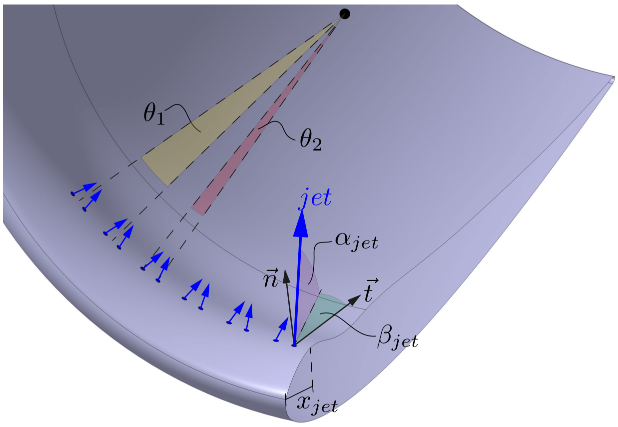

FIG 2. Example of a jet configuration depicted as blue arrows, along with its design parameters θ_1, θ_2, α_{jet}, β_{jet}, and x_{jet}.

Param.	Description	Lower Bound	Upper Bound
N_{jet}	number of jets	10	18
θ_1	spacing of pairs	3°	10°
θ_2	spacing within pair	1°	3°
x_{jet}/l_{int}	location in x-direction	0.10	0.30
d_{jet}/d_{hl}	jet diameter ratio	0.005	$0.008\overline{3}$
U_{jet}/U_∞	velocity ratio	0.3	2
α_{jet}	pitch angle	30°	90°
β_{jet}	skew angle	0°	45°
rot_β	type of rotation	–	–

TAB 2. List of parameters to characterize the AFC system with lower and upper bounds to restrict the parameter space of this study.

diameter of the circular jet is set by d_{jet}/d_{hl}, and the velocity ratio U_{jet}/U_∞ controls the velocity magnitude of the jet U_{jet} normalized by the free-stream velocity U_∞. The pitch angle α_{jet} and the skew angle β_{jet} dictate the spatial orientation of the jets. The parameter α_{jet} denotes a rotation around a vector perpendicular to the plane defined by the surface normal vector $\vec{n}$ and the surface tangent vector $\vec{t}$ parallel to the xz-plane. A pitch angle of $\alpha_{jet} = 90°$ implies a jet in the direction of the surface normal. For $\alpha_{jet} \neq 90°$, an additional rotation around the axis of the surface normal $\vec{n}$ is performed by the angle β_{jet}. The parameter rot_β can be either "co" or "counter". It determines whether the rotation of blowing port pairs around β_{jet} is done in a co-rotating or counter-rotating manner. Counter-rotating implies that jets of pairs face each other. Figure 2 displays a visual representation of the jet rotations.

The parameter space to be investigated in this design study is restricted by upper and lower bounds for each parameter. The nacelle geometry and size are decisive in the choice of boundaries. The blowing ports are located close to the inlet throat, where the thickness of the inlet lip provides sufficient space for the installation of the actuator system. The maximum pressure capacity of fast-switching solenoid valves used in the upcoming wind tunnel model restricts the possible range of jet velocities. Further, geometric complexity should be considered in the design of the blowing ports to ensure practical manufacturing of the AFC module. All parameters of the flow control system and their respective bounds are listed in Table 2.

3. NUMERICAL METHOD

3.1. Flow Control Use Case

The paper at hand investigates the AFC use case of the wing's $C_{L,max}$ condition. This operating condition is crucial in the certification process, and high levels of turbulence and flow separation are expected. The corresponding angle of attack of the engine inlet is taken from Peters et al. [2] and is set to $\alpha = 29°$. Engine nacelles typically encounter higher angles of attack than the wing because of the upwash effect of the wing. Due to the inlet's axisymmetric design, crosswind and angle of attack can be combined and represented by a single angle, α. The free-stream Mach number is fixed at $Ma_\infty = 0.15$ for all simulations. This value is governed by the highest achievable speed in future wind tunnel tests at Wind Tunnel A of the Chair of Aerodynamics and Fluid Mechanics of the Technical University of Munich.

3.2. Numerical Setup

All computations are conducted with the pressure-based flow solver ANSYS Fluent 22R2 using a finite volume method to solve the incompressible Navier-Stokes equations. A steady RANS result serves as an initial solution for Unsteady Reynolds-Averaged Navier-Stokes (URANS) simulations. The SIMPLE algorithm links pressure and velocity, while a momentum-based Rhie-Chow method is employed for mass flux. Convection and diffusion terms in the conservation equations are discretized by a least squares cell-based method. Second-order accurate schemes discretize pressure and the turbulence variables k and ω, while the momentum equation is solved using a bounded central differencing method. Time-dependent calculations are performed by a bounded second-order implicit formulation. A local time-stepping approach with a specified Pseudo Time Courand Number of 5 is selected to adapt the local pseudo time-step size for each cell in the domain. The fixed time-step size is set to $1.6 \cdot 10^{-4}$ s, allowing a maximum of 100 inner iterations per time-step. The Cauchy convergence criterion is specified for the lift and drag coefficients C_L and C_D, reaching convergence if both values meet 10^{-6}. The total simulation time is 0.5 s, with data sampling for time statistics enabled at 0.1 s. Unless otherwise specified, the following results display the averaged values over time. The Courant number for URANS simulations

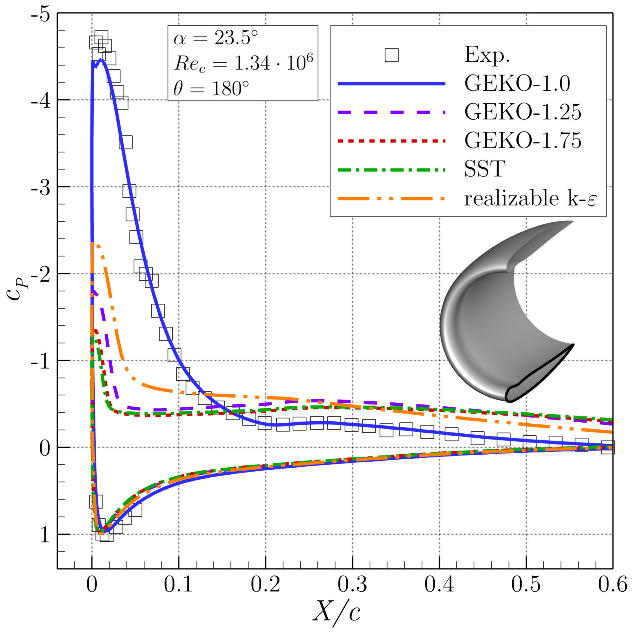

FIG 3. Comparison of c_p-curves with experimental data from [13] simulated with different turbulence models at $\alpha = 23.5°$ and $Re_c = 1.34 \cdot 10^6$

is calculated to be $CFL = 2.4$ based on the fixed time-step chosen. A time-step independence study confirms sufficient temporal resolution to evaluate time-averaged quantities. When comparing time-averaged force coefficients and data from Eqn. 1, 2, and 3 for CFL values of 2.4 and 0.6, the maximum relative error is less than 0.1%.

The numerical setup is validated against experimental data of a flow-through nacelle provided by Schulze and Kähler [13]. After conducting a preliminary grid convergence study on the geometry from Schulze and Kähler, RANS simulations compare the c_p-curves optained applying different turbulence models with experimental data. The chosen angle of attack for validation is 23.5°, which falls within the range where the onset of flow separation occurs at the bottom inlet lip. The c_p-curve is evaluated at the keel line of the nacelle. The comparison of the turbulence models is depicted in Fig. 3. The k-ω GEKO-1.0 model accurately predicts separation behavior and reproduces the suction peak at the bottom inlet lip in agreement with the experiment. Variants of the Generalized k-ω (GEKO) two-equation model differ in the value of the separation parameter C_{SEP}, one of six free parameters available to the user for adjusting the turbulence model without affecting the basic calibration of the model [14]. All URANS simulations of the design study are computed with the k-ω GEKO-1.0 turbulence model.

Because the flow is assumed to be symmetrical, only half of the model is computed with a symmetry boundary condition in the xz-plane. Velocity inlet boundary conditions with velocity components $u = U_\infty \cdot cos(\alpha)$ and $w = U_\infty \cdot sin(\alpha)$ and pressure-outlet boundary conditions define the outer boundaries of the domain.

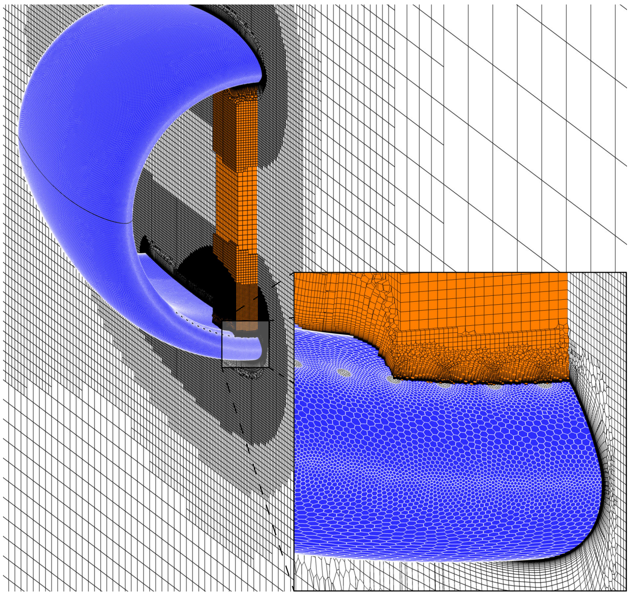

FIG 4. Overview of the Poly-Hexcore grid structure with a detailed view of the prism layers near the blowing ports.

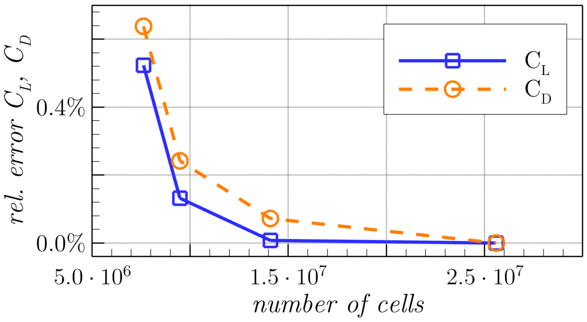

FIG 5. Results of the grid convergence study with four different grid sizes.

The turbulence intensity is set to 1%. Without including a nozzle geometry at the blowing ports, the jets are also implemented using velocity-inlet boundary conditions. The additional modeling of the nozzles (resulting in an increased computational cost) is omitted in favor of a higher total number of simulations. The box-shaped computational domain measures 25c×5c×13c (length×width×height), with the nacelle placed 5c downstream of the front face and 5c above the bottom face of the domain. The computational grid, shown in Fig. 4, is created using the ANSYS Fluent Meshing grid generator. A Poly-Hexcore grid structure combines high-quality octree hexahedron cells in the bulk region with isotropic poly-prisms in the boundary layer. Zore et al. [15] demonstrate that this mosaic meshing technology can reduce total cell count and computation time while maintaining high accuracy. To ensure proper capture of crucial flow features, refinement regions are designated near the nacelle, at the bottom inlet section, and in the wake. The surface mesh shows high levels of detail at the nacelle's leading and trailing edge and at the blowing ports. The boundary layer is resolved using 40 prism layers, a first cell height of 0.003 mm, and a stretching ratio of 1.2, resulting in a y^+-value of $y^+ < 1$ for the entire domain. The grid size is determined by conducting a grid convergence study on the baseline AFC configuration, described in Section 4. The time-averaged integral lift coefficient C_L and drag coefficient C_D are the decisive parameters. A factor of $1/\sqrt{2}$ alters the cell size in the surface and volume mesh, while the first cell height and the number of prism layers are unaffected. Figure 5 plots the error of the force coefficients relative to the extra-fine mesh with 25.6 million cells when using the mesh sizes coarse, medium, fine, and extra-fine. For the design study, the fine mesh with around 14.1 million cells is the most appropriate option as it has a relative error below 0.1% for both force coefficients.

4. RESULTS AND DISCUSSION

All results shown are based on simulations conducted at an angle of attack of $\alpha = 29°$ and a Mach number of $Ma_\infty = 0.15$. The Reynolds number calculated with the chord length of the nacelle gives $Re_c = 2.83 \cdot 10^6$, which corresponds to a free-stream velocity of $U_\infty = 51$ m/s. Results were calculated from time-averaged simulation data.

4.1. Sensitivity Analysis and Optimization

In the following, the computational results of a sensitivity analysis and a three-step design optimization of the AFC system are presented and discussed. Starting point of the sensitivity analysis is a baseline configuration defined by its parameter vector

$$\vec{g}_{bl} = \begin{bmatrix} N_{jet} \\ \theta_1 \\ \theta_2 \\ x_{jet}/l_{int} \\ d_{jet}/d_{hl} \\ U_{jet}/U_\infty \\ \alpha_{jet} \\ \beta_{jet} \\ rot_\beta \end{bmatrix} = \begin{bmatrix} 14 \\ 6° \\ 3° \\ 0.15 \\ 0.00\overline{6} \\ 1 \\ 90° \\ 0° \\ \text{undef.} \end{bmatrix}.$$

For the initial sensitivity analysis, the skew angle β_{jet} is set to 0°, resulting in an undefined rot_β. The remaining seven parameters are altered within their predefined bounds (see Table 2). One parameter at a time is changed, to analyze its isolated effect on the quantities of η_σ, DC_{60}, and SC_{60}.

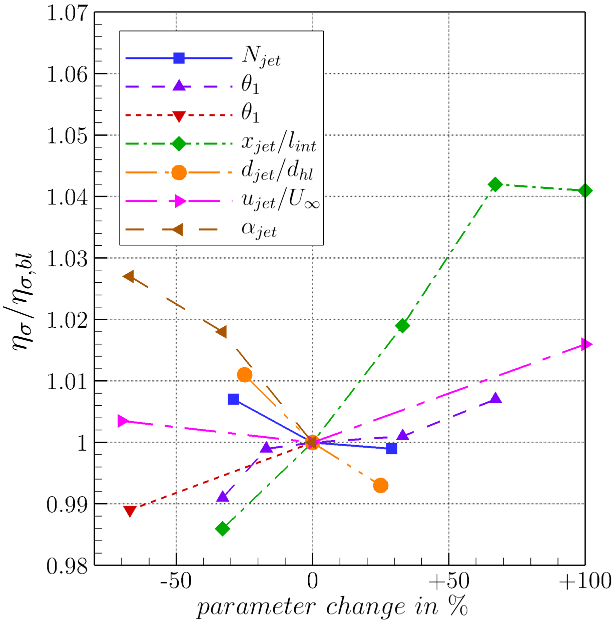

FIG 6. Sensitivity analysis of the parameters N_{jet}, θ_1, θ_2, x_{jet}/l_{int}, d_{jet}/d_{hl}, U_{jet}/U_∞, and α_{jet} on the pressure recovery coefficient η_σ.

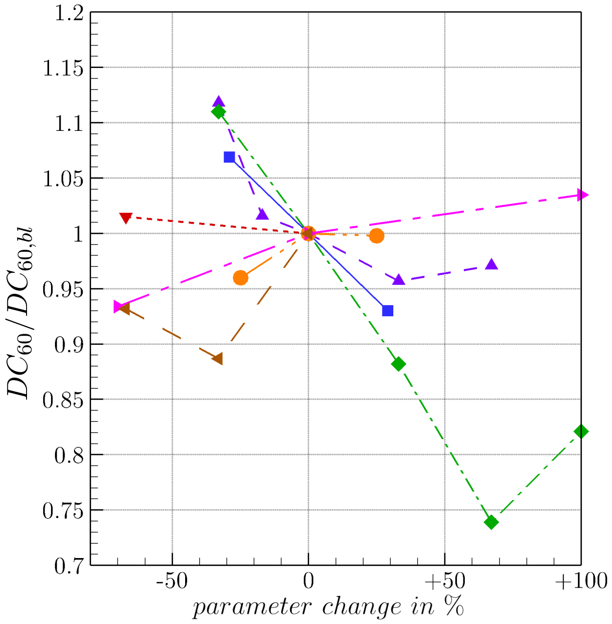

FIG 7. Sensitivity analysis of the parameters N_{jet}, θ_1, θ_2, x_{jet}/l_{int}, d_{jet}/d_{hl}, U_{jet}/U_∞, and α_{jet} on the distortion coefficient DC_{60}.

In Figs. 6-8, the changes in η_σ, DC_{60}, and SC_{60} relative to the baseline configuration are displayed as the parameters of the AFC system are altered. On the horizontal axis, the percentage change of parameters with respect to the baseline configuration is plotted. For the pressure recovery coefficient η_σ, a value greater than 1 indicates an improvement compared to the baseline configuration, while a value below 1 implies a decrease which is desirable for the coefficients DC_{60} and SC_{60}. Results reveal that the parameter for the x-position of the blowing ports x_{jet}/l_{int} significantly influences all three evaluation quantities. Best values are obtained when x_{jet}/l_{int} is either 0.25 or 0.30. This corresponds to an increase relative to the baseline configuration of 66.7% and 100%, respectively. The throat of the inlet is located at $x/l_{int} = 0.27$, meaning the farthest downstream x-position is already downstream of the throat. It is important to consider that when blowing is performed perpendicular to the surface, the x-position of the ports also affects the local slope of the surface and,

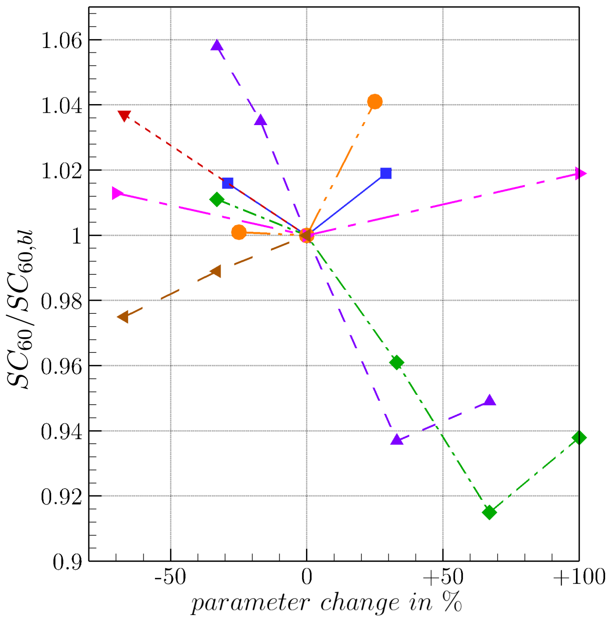

FIG 8. Sensitivity analysis of the parameters N_{jet}, θ_1, θ_2, x_{jet}/l_{int}, d_{jet}/d_{hl}, U_{jet}/U_∞, and α_{jet} on the swirl coefficient SC_{60}.

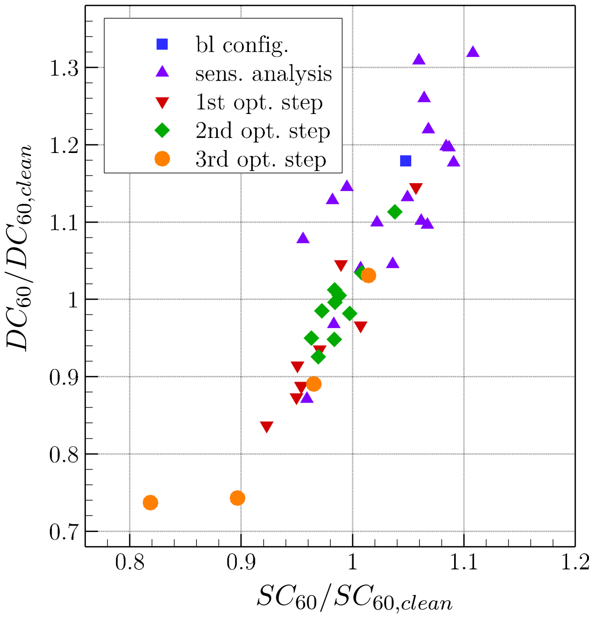

FIG 9. Plot of DC_{60} and SC_{60} coefficients of all test cases normalized by values of the clean nacelle configuration without AFC.

thus, changes the direction of the jets.

As shown in Fig. 6, increasing x_{jet}/l_{int} provides the most benefit to the pressure recovery coefficient η_σ with more than 4% improvement relative to the baseline case. Reducing the pitch angle α_{jet} also improves η_σ by increasing the momentum input of the AFC system in x-direction. Other parameters show only a minor influence on η_σ with a relative change below 2%. The distortion coefficient DC_{60} improves by up to 26% relative to the baseline configuration as the x-position of the blowing ports moves further downstream, as depicted in Fig. 7. By increasing N_{jet} or reducing U_{jet}/U_∞ or α_{jet}, the distortion coefficient improves by more than 5%. Effects of parameters on the swirl coefficient SC_{60} are plotted in Fig. 8. By increasing θ_1 or x_{jet}/l_{int} or decreasing α_{jet}, improvements in the swirl coefficient relative to the baseline configuration can be achieved. The changes of the coefficients DC_{60} and SC_{60} with the x-position of the blowing ports x_{jet}/l_{int} show a similar pattern.

The decision variable for the remainder of the design study is the distortion coefficient DC_{60}, which is most sensitive to parameter changes. Based on the sensitivity analysis, an optimized position of the blowing ports shows the most potential to improve the performance of the AFC system. As the first step of optimization, combinations of parameters $(N_{jet}, \theta_1) = \{(18,6°), (16,8°), (14,10°)\}$ are tested at x-positions $x_{jet}/l_{int} = \{0.20, 0.25, 0.30\}$ with θ_2 fixed at 3° due to its minimal impact on the system's performance. For now, all other parameters are using the baseline values. Combinations were selected to have a uniform distribution within the parameter bounds and a similar overall extent of the blowing ports in circumferential direction. The arrangement of the blowing ports $(N_{jet}, \theta_1) = (18,6°)$ at the x-position $x_{jet}/l_{int} = 0.30$ yields the largest improvement relative to the baseline configuration with 29.0%. The parameters responsible for the number and positioning of the blowing ports are set at $(N_{jet}, \theta_1, \theta_2, x_{jet}/l_{int}) = (18,6°,3°,0.30)$. The next step is to test all combinations of the parameters $\alpha_{jet} = \{30°, 60°\}$, $\beta_{jet} = \{0°, 22.5°, 45°\}$, and $rot_\beta = \{\text{co}, \text{counter}\}$ to optimize the jet's spatial orientation. None of the ten possible parameter combinations produces any improvement, so the baseline values are fixed, and blowing is performed in surface normal direction. In the third optimization step, the parameter for the jet velocity ratio is varied within the defined bounds with $U_{jet}/U_\infty = \{0.3, 0.8, 1.5, 2.0\}$. The best flow quality at the AIP is achieved with a jet velocity ratio of $U_{jet}/U_\infty = 2.0$, resulting in a 37.5% improvement in distortion coefficient DC_{60} compared to the baseline configuration. Further, the pressure recovery coefficient η_σ is improved by 6.7%, and the swirl coefficient SC_{60} by 21.9%. The results of the design study suggest an optimized parameter vector for the AFC system of

$$\vec{g}_{opt} = \begin{bmatrix} N_{jet} \\ \theta_1 \\ \theta_2 \\ x_{jet}/l_{int} \\ d_{jet}/d_{hl} \\ U_{jet}/U_\infty \\ \alpha_{jet} \\ \beta_{jet} \\ rot_\beta \end{bmatrix} = \begin{bmatrix} 18 \\ 6° \\ 3° \\ 0.30 \\ 0.00\overline{6} \\ 2 \\ 90° \\ 0° \\ \text{undef.} \end{bmatrix}.$$

Figure 9 provides an overview of the evolution of the coefficients DC_{60} and SC_{60} throughout the design study. Here, the coefficients are normalized by the values of the clean configuration without AFC to display the actual benefit of the system. The baseline configuration and several other test cases offer no advantage in distortion or swirl coefficient. The point cloud in Fig. 9 shows a linear shape, confirming a positive correlation between the coefficients DC_{60} and SC_{60}. The optimized configuration of the AFC system found in this design study can improve the pressure recovery coefficient η_σ by 3.2%, the distortion coefficient DC_{60} by 26.3%, and the swirl coefficient by 18.2% compared to the clean configuration without AFC.

4.2. Flow Field Analysis

The following flow field analysis reveals differences in the flow of the clean, baseline, and optimized AFC configurations. Further, a detailed view on the region downstream of the blowing ports provides first clues about existing flow mechanisms provoked by AFC.

The evaluation quantities η_σ and DC_{60} are directly related to the total pressure loss at the AIP and its circumferential distribution. Figures 10 and 11 compare the non-dimensional total pressure at the AIP for the clean and optimized or baseline and optimized configurations, respectively. A form equivalent to the pressure recovery coefficient η_σ is chosen for better visualization. All configurations, clean, baseline, and optimized, show a region of substantial pressure loss at the bottom inlet lip because of flow separation. In agreement with the values for η_σ and DC_{60}, the optimized AFC configuration features a smaller region of total pressure loss than the clean configuration, while for the baseline configuration the region of total pressure loss increases. The optimized configuration shows a less sharp transition between regions of high pressure loss and undisturbed flow. For the clean configuration, the smooth contours of the region of high pressure loss suggest a separation bubble of a pressure-induced flow separation. In contrast, the baseline and optimized configurations show wavy to vortex-like structures in their regions of total pressure loss. An apparent circular structure can be seen on the optimized configuration's left edge.

In Fig. 12 and Fig. 13, isosurfaces represent the size and shape of the separation bubbles for the configurations clean, baseline, and optimized. The isosurfaces correspond to a zero x-velocity component $u/U_\infty = 0$. The clean configuration in Fig. 12 shows a wide separation bubble. The separation line shifts downstream from $x/l_{int} = 0.18$ near the keel line to $x/l_{int} = 0.35$ at the outer edge. Although the optimized AFC configuration cannot prevent separation, it limits the size of the separation bubble to a much smaller area at the bottom inlet lip. A small region of flow separation is also visible near the outer blowing port of the optimized configuration. The isosurface of the baseline configuration in Fig. 13 confirms an expansion of the separation bubble relative to the clean nacelle configuration. Positioning the blowing ports in front of the separation line, combined with blowing in surface normal direction, leads to a destabilization of the boundary layer and large-scale flow separation structures.

To identify the reasons for the varying impact of AFC, a detailed analysis of the flow near the blowing ports is necessary. Figures 14 and 15 show the x-vorticity ω_x normalized by the highlight ra-

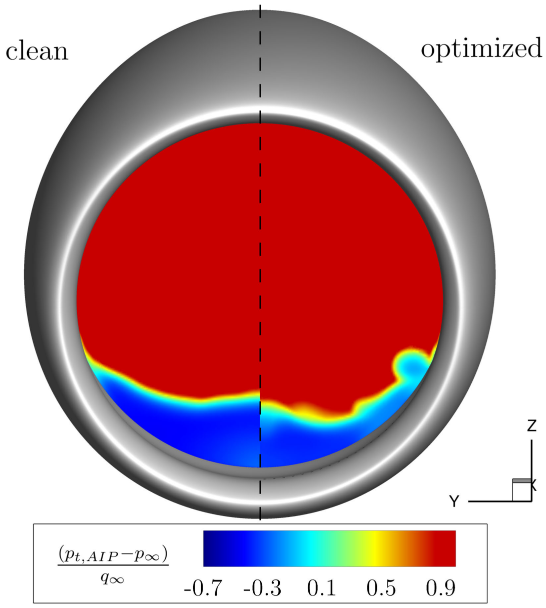

FIG 10. Comparison of the non-dimensional total pressure at the AIP of the clean (left) and optimized (right) configuration.

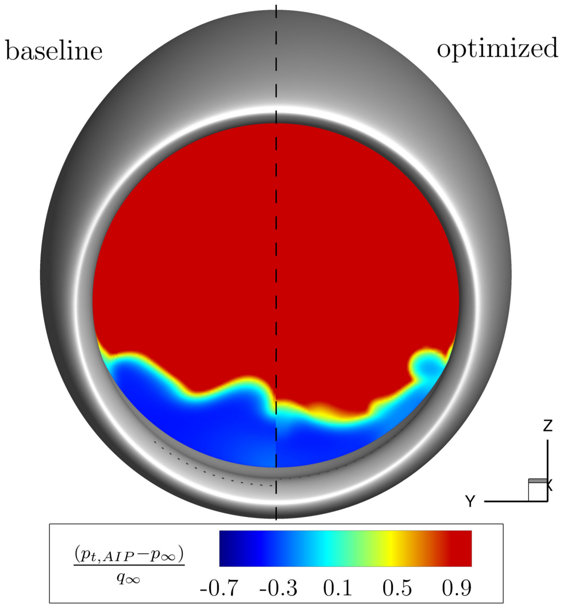

FIG 11. Comparison of the non-dimensional total pressure at the AIP of the baseline (left) and optimized (right) configuration.

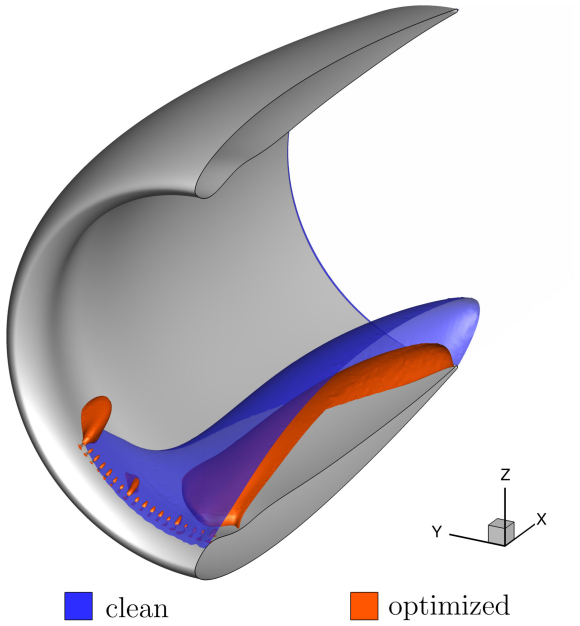

FIG 12. Comparison of separation bubbles of the clean (blue) and optimized (orange) configuration, represented by isosurfaces at $u/U_\infty = 0$.

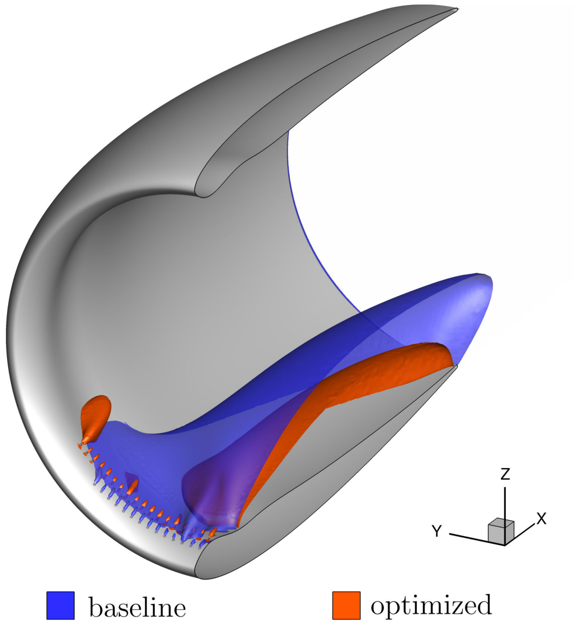

FIG 13. Comparison of separation bubbles of the baseline (blue) and optimized (orange) configuration, represented by isosurfaces at $u/U_\infty = 0$.

dius r_{hl} and the free-stream velocity U_∞ at x-slices $x/l_{int} = 0.31$ and $x/l_{int} = 0.34$, respectively. So, the x-slices are located at distances $\Delta x/l_{int} = 0.01$ and $\Delta x/l_{int} = 0.04$ downstream of the jets. Arrows represent the cross-flow velocity vectors in the x-slices. Counter-rotating vortex pairs (CVP) form downstream of the cylindrical jets at $x/l_{int} = 0.31$ visible by high levels of vorticity in Fig.14. The rotational direction of each CVP points outward, and vortices of adjacent jets rotate towards each other. The coherent vortical structures propagate futher downstream and are still visible at $x/l_{int} = 0.34$ in Fig. 15. The CVPs transport momentum into layers close to the wall, leading to an energized boundary layer and delayed flow separation. The formation of CVPs is also described by Cambonie et al. [16], who experimentally studied circular flush jets in cross-flow in a water tunnel at velocity ratios of U_{jet}/U_∞ from 0.5 to 3. The authors attribute the formation of CVPs to an induced vertical velocity component in the center of the deflected jet and a roll-up of the jet's shear layer. Figures 16 and 17 show the normalized x-vorticity and velocity vectors of the baseline configuration at equal distances downstream of the jets. The two configurations, baseline and optimized, differ by the parameters N_{jet}, x_{jet}/l_{int}, and U_{jet}/U_∞ as described in Section 4.1. In contrast to the optimized variant, the baseline configuration does not exhibit increased x-vorticity values. A distinct formation of CVPs is not observed at $x/l_{int} = 0.16$ or $x/l_{int} = 0.19$. If blowing ports are positioned in front of the throat, an increased radial component of the velocity counteracts the rotation of the CVP. Analyses of the intermediate optimization results show that CVPs start developing along the x-axis for $x_{jet}/l_{int} > 0.25$ when blowing in surface normal direction ($\alpha_{jet} = 90°$, $\beta_{jet} = 0°$) with a constant circumferential spacing of 3° between blowing ports ($\theta_1 = 6°$, $\theta_2 = 3°$). CVPs form when the velocity ratio of the jets U_{jet}/U_∞ is higher than 0.8. The angular spacing of adjacent jets must be sufficiently large to allow the formation of CVPs.

5. CONCLUSION

The present design study on an innovative AFC system to improve inlet performance consisted of a sensitivity analysis of predefined parameters of the AFC system and a stepwise optimization. The AFC system was tested on the inlet of a generic UHBR engine nacelle designed as a flow-through nacelle. An URANS approach provides sufficient spatial and temporal resolution of unsteady phenomena at a stalling inlet, while the computational effort per test case was low enough, allowing evaluation of many configurations. The inlet performance was evaluated using the quantities pressure recovery coefficient η_σ, distortion coefficient DC_{60}, and swirl coefficient SC_{60}. An angle of attack of $\alpha = 29°$ at a Mach number of $Ma_\infty = 0.15$ represented the use case of the design study. All jets were circular in cross-section, blowing at constant jet velocities over time.

The sensitivity analysis revealed that changes in the x-position of the blowing ports have the most significant impact on all evaluation quantities. Blowing is most effective in the throat area, where the jet hits the main flow at a right angle. Stepwise parameter optimization improved the pressure recovery coefficient η_σ by 3.2%, the distortion coefficient DC_{60} by 26.3%, and the swirl coefficient SC_{60} by 18.2% relative to the clean configuration without AFC. Due to mutual dependencies of parameters and a limited number of test cases, the optimized parameter set found most

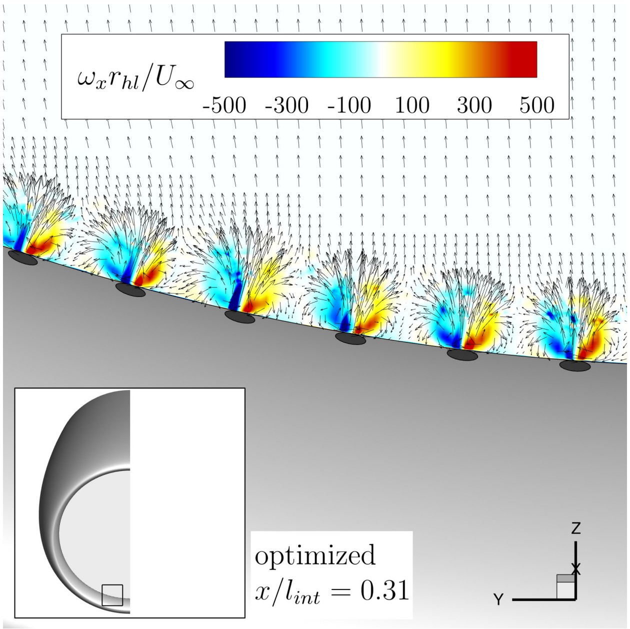

FIG 14. Plot of the normalized x-component of the vorticity and the tangential velocity vectors at the x-slice at $x/l_{int} = 0.31$ of the optimized configuration.

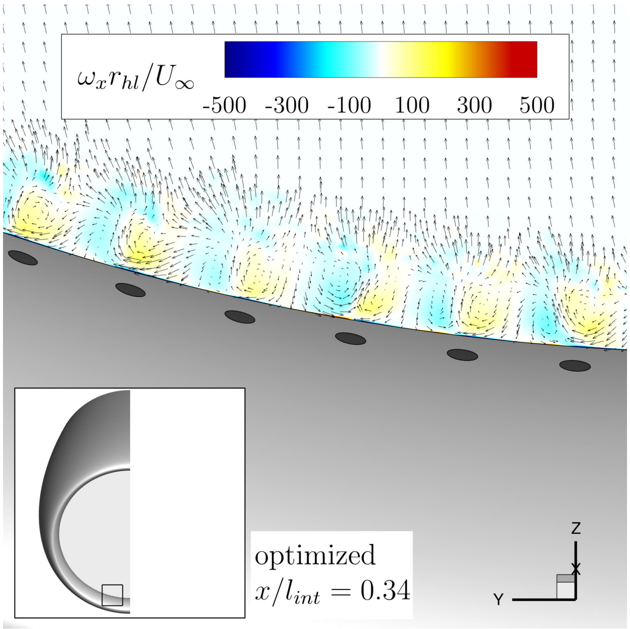

FIG 15. Plot of the normalized x-component of the vorticity and the tangential velocity vectors at the x-slice at $x/l_{int} = 0.34$ of the optimized configuration.

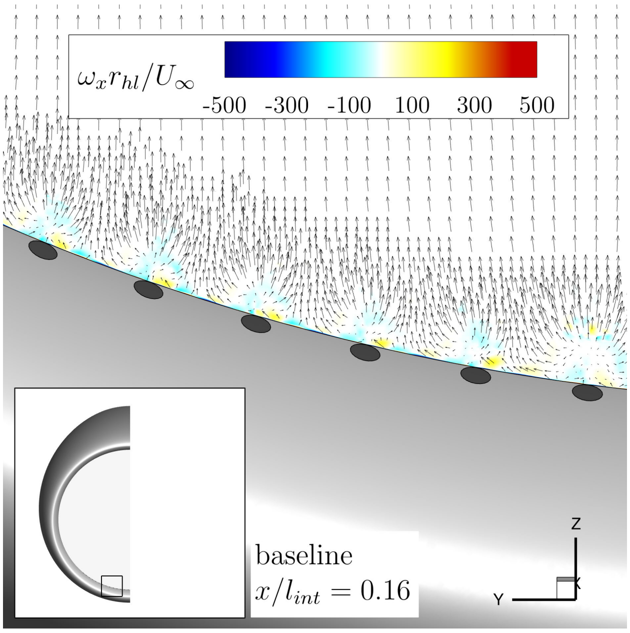

FIG 16. Plot of the normalized x-component of the vorticity and the tangential velocity vectors at the x-slice at $x/l_{int} = 0.16$ of the baseline configuration.

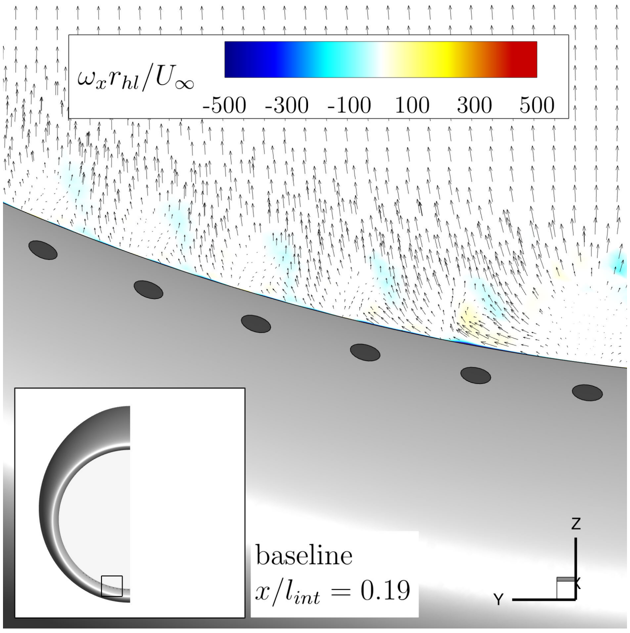

FIG 17. Plot of the normalized x-component of the vorticity and the tangential velocity vectors at the x-slice at $x/l_{int} = 0.19$ of the baseline configuration.

likely does not represent a global optimum in the parameter space. Instead, this design study aimed to assess the influence of parameters and define a reasonable parameter set for the design of a future wind tunnel model.

Analyzing the flow field downstream of the blowing ports gave first insights into the effects of AFC at the inlet of UHBR engine nacelles. Given a proper choice of parameters, distinct pairs of counter-rotating vortices form downstream of each jet. This investigation found that vortex formation is favored when blowing is performed perpendicular to the local surface and the ports are placed in close proximity to the inlet throat. The formation and strength of these vortices are directly linked to the improvement in inlet performance.

The next steps in this research project are to develop a wind tunnel model for experimental investigations of AFC on inlet flows and to extend the validation database for future numerical work. Scale-resolved simulations of inlet flows with AFC allow a more detailed analysis of vortical structures produced by the system.

ACKNOWLEDGMENTS

The funding of this work by the BMWK within the LuFo VI-2 project AKTIVER (Aktive Strömungsbeeinflussung in Verdichterkomponenten künftiger Flugantriebe, FKZ: 20E2113A) is gratefully acknowledged. Further, the authors want to thank ANSYS for providing the simulation software used for this numerical investigation and the Leibniz Supercomputing Center (LRZ, www.lrz.de) for providing computing time on the LRZ Linux-Cluster.

Contact address:

stefan.hayboeck@tum.de

References

[1] Richard A. Zimbrick and Jeffrey L. Colehour. Investigation of very high bypass ratio engines for subsonic transports. *Journal of Propulsion and Power*, 6(4):490–496, 1990. DOI: 10.2514/3.25461.

[2] Andreas Peters, Zoltán S. Spakovszky, Wesley K. Lord, and Becky Rose. Ultra-Short Nacelles for Low Fan Pressure Ratio Propulsors. In *ASME Turbo Expo 2014: Turbine Technical Conference and Exposition*, Düsseldorf, 2014. American Society of Mechanical Engineers. DOI: 10.1115/GT2014-26369.

[3] Chris Freeman and Arthur L. Rowe. Intake Engine Interactions of a Modern Large Turbofan Engine. In *International Gas Turbine and Aeroengine Congress and Exhibition*, Indianapolis, Indiana, jun 1999. American Society of Mechanical Engineers. DOI: 10.1115/99-GT-344.

[4] Kuen-Bae Lee, Mark Wilson, and Mehdi Vahdati. Effects of Inlet Disturbances on Fan Stability. *Journal of Engineering for Gas Turbines and Power*, 141(5), 2019. DOI: 10.1115/1.4042204.

[5] David R. Williams and Douglas G. MacMynowski. Brief History of Flow Control. In *Fundamentals and Applications of Modern Flow Control*. American Institute of Aeronautics and Astronautics, Reston ,Virginia, 2009. DOI: 10.2514/5.9781563479892.0001.0020.

[6] R.W. Guo and J. Seddon. The Swirl in an S-Duct of Typical Air Intake Proportions. *Aeronautical Quarterly*, 34(2):99–129, 1983. DOI: 10.1017/S0001925900009641.

[7] Susan Gorton, Lewis Owens, Luther Jenkins, Brian Allan, and Ernest Schuster. Active Flow Control on a Boundary-Layer-Ingesting Inlet. In *42nd AIAA Aerospace Sciences Meeting and Exhibit*, Reston, Virigina, 2004. American Institute of Aeronautics and Astronautics. DOI: 10.2514/6.2004-1203.

[8] Anne-Laure Delot, Eric Garnier, and Didier Pagan. Flow Control in a High-Offset Subsonic Air Intake. In *47th AIAA/ASME/SAE/ASEE Joint Propulsion Conference & Exhibit*, San Diego, 2011. American Institute of Aeronautics and Astronautics. DOI: 10.2514/6.2011-5569.

[9] Eric Garnier. Flow Control by Pulsed Jet in a Curved S-Duct: A Spectral Analysis. *AIAA Journal*, 53(10):2813–2827, 2015. DOI: 10.2514/1.J053422.

[10] Vinayak R. Nambiar and Vassilios Pachidis. Nacelle intake flow separation reduction at cruise condition using active flow control. *Propulsion and Power Research*, 11(3):337–352, 2022. DOI: 10.1016/j.jppr.2022.07.005.

[11] Robert Christie, Alexander Heidebrecht, and David MacManus. An automated approach to nacelle parameterization using intuitive class shape transformation curves. *Journal of Engineering for Gas Turbines and Power*, 139(6), 2017. DOI: 10.1115/1.4035283.

[12] Brenda Kulfan and John Bussoletti. "Fundamental" Parameteric Geometry Representations for Aircraft Component Shapes. In *11th AIAA/ISSMO Multidisciplinary Analysis and Optimization Conference*, pages 547–591, Reston, Virigina, 2006. American Institute of Aeronautics and Astronautics. DOI: 10.2514/6.2006-6948.

[13] Sonja Schulze and Christian J. Kaehler. Analysis of the Flow in Stalling Engine Inlet Models with Different Visualization and Measurement Techniques. In *Second Symposium "Simulation of Wing and Nacelle Stall"*, Braunschweig, 2010.

[14] Florian R. Menter, Alexey Matyushenko, and Richard Lechner. Development of a Generalized K-ω Two-Equation Turbulence Model. In *Notes on Numerical Fluid Mechanics and Multidisciplinary Design*, volume 142, pages 101–109. 2020. DOI: 10.1007/978-3-030-25253-3_10.

[15] Krishna Zore, Balasubramanyam Sasanapuri, Gandhar Parkhi, and Alan Varghese. ANSYS MOSAIC POLY-HEXCORE MESH FOR HIGH-LIFT AIRCRAFT CONFIGURATION. In *21st AeSI Annual CFD Symposium*, Bangalore, India, 2019.

[16] Tristan Cambonie, Nicolas Gautier, and Jean-Luc Aider. Experimental study of counter-rotating vortex pair trajectories induced by a round jet in cross-flow at low velocity ratios. *Experiments in Fluids*, 54(3):1475, mar 2013. DOI: 10.1007/s00348-013-1475-9.